Journal of Geophysical Research: Oceans

RESEARCH ARTICLE
10.1002/2017JC013252

Direct Measurements of Mean Reynolds Stress and Ripple Roughness in the Presence of Energetic Forcing by Surface Waves

Malcolm E. Scully[1], John H. Trowbridge[1], Christopher R. Sherwood[2], Katie R. Jones[1], and Peter Traykovski[1]

[1]Applied Ocean Physics and Engineering Department, Woods Hole Oceanographic Institution, Woods Hole, MA 02543, USA, [2]Coastal and Marine Geology, U.S Geological Survey, Woods Hole, MA, USA

Key Points:
- Covariance measurements of Reynolds stress are consistent with boundary layer models of wave-current interaction if bed roughness is known
- The drag experienced by the mean flow on wave-exposed continental shelves can vary significantly in time and space
- Drag depends on nonequilibrium ripple dynamics, ripple anisotropy, and the orientation of the ripples relative to the current

Correspondence to:
M. E. Scully,
mscully@whoi.edu

Citation:
Scully, M. E., Trowbridge, J. H., Sherwood, C. R., Jones, K. R., & Traykovski, P. (2018). Direct measurements of mean reynolds stress and ripple roughness in the presence of energetic forcing by surface waves. *Journal of Geophysical Research: Oceans*, *123*, 2494–2512. https://doi.org/10.1002/2017JC013252

Received 11 JUL 2017
Accepted 7 OCT 2017
Accepted article online 26 MAR 2018
Published online 10 APR 2018

Abstract Direct covariance observations of the mean flow Reynolds stress and sonar images of the seafloor collected on a wave-exposed inner continental shelf demonstrate that the drag exerted by the seabed on the overlying flow is consistent with boundary layer models for wave-current interaction, provided that the orientation and anisotropy of the bed roughness are appropriately quantified. Large spatial and temporal variations in drag result from nonequilibrium ripple dynamics, ripple anisotropy, and the orientation of the ripples relative to the current. At a location in coarse sand characterized by large two-dimensional orbital ripples, the observed drag shows a strong dependence on the relative orientation of the mean current to the ripple crests. At a contrasting location in fine sand, where more isotropic sub-orbital ripples are observed, the sensitivity of the current to the orientation of the ripples is reduced. Further, at the coarse site under conditions when the currents are parallel to the ripple crests and the wave orbital diameter is smaller than the wavelength of the relic orbital ripples, the flow becomes hydraulically smooth. This transition is not observed at the fine site, where the observed wave orbital diameter is always greater than the wavelength of the observed sub-orbital ripples. Paradoxically, the dominant along-shelf flows often experience lower drag at the coarse site than at the fine site, despite the larger ripples, highlighting the complex dynamics controlling drag in wave-exposed environments with heterogeneous roughness.

1. Introduction

The drag that the seafloor exerts on the overlying flow fundamentally controls a wide range of transport processes in the coastal ocean. Longstanding bottom boundary layer models indicate that the boundary stress is affected both by wave-current interaction in the centimeters-thick wave boundary layer (Grant & Madsen, 1979, 1986; Styles & Glenn, 2000, 2002; Wiberg & Smith, 1983), as well as the presence of bedforms and flow-bedform interaction (Grant & Madsen, 1982, 1986; Traykovski, 2007; Wiberg & Harris, 1994). While these models have existed for nearly four decades, most field tests of their validity have been based on log-profile or inertial-range estimates of the bottom stress (Grant et al., 1984; Green et al., 1990; Gross et al., 1994; Huntley, 1988; Sherwood et al., 2006; Wiberg & Smith, 1983). Direct covariance measurements of near bed momentum flux, combined with quantitative observations of the seafloor roughness are rare (e.g., Sherwood, 2011) and have not produced a coherent relationship between morphology, flow directions, and bottom roughness.

Despite the importance of the parameterization of bottom stress in coastal circulation models, in many applications the bottom drag is simply treated as a tuning parameter that is adjusted to best match observations. The importance of wave-current interaction on the bottom drag has been demonstrated in idealized numerical simulations of coastal and estuarine flows (Davies & Lawrence, 1995; Signell et al., 1990; Xie et al., 2001). However, simulations with realistic forcing that allow the bottom drag coefficient to vary in a manner consistent with existing models for wave-current interaction show lower skill compared to simulations using simpler drag laws (Ganju & Sherwood, 2010). These results highlight the need for comprehensive measurements to fully evaluate existing boundary layer models.

There are a number of reasons why existing boundary layer models may fail. Density stratification caused by suspended sediment (Agrawal & Traykovski, 2001; Trowbridge & Kineke, 1994) or by heat and salt (Lentz

et al., 1999; Trowbridge & Elgar, 2003) can be dynamically important near the seafloor and these gradients must be accurately measured. Full water column Langmuir cells (Gargett & Wells, 2007; Gargett et al., 2004) have been suggested to disrupt the near-bottom log-layer and influence the bottom drag (Tejada-Martinez et al., 2012). Field measurements obtained over rippled beds by particle image velocimetry (Hackett et al., 2009; Luznik et al., 2007; Nimmo-Smith et al., 2002) indicate flow structures within the wave boundary layer that are more complex than the assumed one-dimensional models of wave-current-seabed interaction.

In this paper we present direct covariance measurements of mean flow Reynolds stress combined with direct measurements of the seafloor roughness with the goal of testing commonly used wave-current boundary layer models. The model equations are presented in section 2 and description of the instrumentation and analytical methods follows in section 3. The results are presented in section 4, followed by a discussion (section 5), and summary and conclusions (section 6).

2. Model Equations

The primary goal of this paper is to test existing boundary layer models that include wave-current interaction and dynamic bed roughness. In the section below, we present the theoretical background and the basic equations that are used in our analysis. A more complete review of this material can be found in a text (e.g., Soulsby, 1997) or review article (e.g., Trowbridge & Lentz, 2017) on bottom boundary layer processes.

A fundamental assumption is that above the region immediately adjacent to the seafloor where viscosity (ν) is important, there is a constant stress layer in an unstratified bottom boundary layer where the turbulent Reynolds stress is approximately equal to the boundary shear stress (τ_b). In this region, in the absence of waves, the appropriate velocity scale is the bottom shear velocity $u_{*c}=\sqrt{\tau_b/\rho_0}$, and dimensional consideration demonstrates that the mean current velocity (U) is logarithmically distributed in the vertical:

$$U(z)=\frac{u_{*c}}{\kappa}\log\left(\frac{z}{z_0}\right) \tag{1}$$

where κ is the von Karman constant ($\sim$0.4) and z_0 is the hydrodynamic roughness; the height where the velocity profile reaches zero by definition. This logarithmic distribution of velocity is valid for the region above the viscous sub-layer ($\delta_\nu=10.7\nu/u_{*c}$) but sufficiently close to the bottom so that the vertical distribution of the shear stress is approximately constant. The vertical extent of this constant stress layer is typically $\sim$10% of the current boundary layer thickness (δ_c). The boundary shear stress is often parameterized using a drag coefficient (C_d):

$$\tau_b=-\rho_0\langle u_1' u_3'\rangle=C_d\rho_0|U|U \tag{2}$$

where the angled brackets indicate Reynolds averaging and the primes indicate turbulent fluctuation of velocity. For a simple steady flow where (1) is valid and vertical density stratification is absent, C_d can be expressed as:

$$C_d=\left[\frac{\kappa}{\log\left(z/z_0\right)}\right]^2 \tag{3}$$

The value of z_0 depends on the ratio of the average height of the surface roughness elements to δ_ν, which is referred to as the boundary Reynolds number ($R_*=k_s u_{*c}/\nu$). When $R_*<5$, the flow is hydraulically smooth and the height of the roughness elements is smaller than δ_ν. When $R_*>70$, the flow is hydraulically rough and the roughness elements protrude above the viscous sub-layer. For a plane bed, where the dominant roughness elements are the individual sediment grains (with median diameter denoted as D_{50}), values of z_0 are given by:

$$z_0=\begin{Bmatrix}\dfrac{\nu}{9u_{*c}} & R_*<5\\ \dfrac{D_{50}}{30} & R_*>70\end{Bmatrix} \tag{4}$$

The above relationships are complicated in a number of ways by the presence of energetic orbital motions associated with surface gravity waves. The highly sheared oscillatory boundary layer flows driven by waves

enhance the drag that is felt by the overlying current. Grant and Madsen (1979), hereafter referred to as GM-79, proposed a one-dimensional time-dependent model that incorporates the combined effects of a steady current in the presence of oscillatory waves. GM-79 parameterizes this combined effect within the so-called wave-current boundary layer, by employing a shear velocity u_{*cw} that characterizes the maximum bed stress associated with the combined wave and current motions:

$$u_{cw} = u_{*w}\left[1 + 2(u_{*c}/u_{*w})^2 \cos\phi + (u_{*c}/u_{*w})^4\right]^{1/4} \tag{5}$$

where ϕ is the angle between the current and direction of wave propagation and u_{*w} is the friction velocity associated with the wave-induced shear stress (τ_w) given as:

$$u_{*w}^2 = \frac{\tau_w}{\rho_0} = \frac{\kappa u_{*cw} u_b}{\sqrt{\left[\log\left(\frac{\kappa u_{*cw}}{z_0 \omega}\right) - 1.15\right]^2 + \left(\frac{\pi}{2}\right)^2}} \tag{6}$$

where u_b is the near-bed wave-induced velocity, and ω is the dominant frequency of the surface waves. In the region above the wave-current boundary layer ($z > \delta_{cw} = \kappa u_{*cw}/\omega$), the effect of the wave-current interaction is to increase the apparent roughness experienced by the current so that equation (1) becomes:

$$U(z) = \frac{u_{*c}}{\kappa}\left(\frac{u_{*c}}{u_{*cw}} \log\frac{\delta_{cw}}{z_0} + \log\frac{z}{\delta_{cw}}\right) \tag{7}$$

Equations (5–7) are solved iteratively using the observed wave and current parameters and prescribing a suitable bed roughness. While a number of modifications to GM-79 have been proposed, including accounting for the presence of vertical density stratification (Glenn & Grant, 1987; Styles & Glenn, 2000, 2002), this basic framework still is used to quantify the drag due to the combined effects of waves and currents in coastal flows.

Application of the GM-79 model requires knowledge of z_0. In sandy wave-influenced environments, the bed roughness is influenced by wave-formed ripples. These ripples are typically quantified in terms of their height (η) and wavelength (λ). The roughness associated with these ripples is often assumed to be:

$$z_0^{rip} = a_r \frac{\eta^2}{\lambda} \tag{8}$$

where a_r is a coefficient in the range of 0.3 – 3 (Soulsby, 1997). In the results presented below, we use a value of $a_r = 0.3$, which agrees most favorably with our best model for C_d. While there are numerous proposed formulations for λ and η (e.g., Nelson et al., 2013), one of the most commonly used models is that of Wiberg and Harris (1994) (hereafter referred to as WH-94). Following the work of Clifton and Dingler (1984), WH-94 identify three types of ripples based on the ratio of the near-bed wave orbital diameter (d_0) to grain size (D_{50}). For small values of d_0/D_{50}, large orbital ripples are observed where $\lambda \propto d_0$. For large values of d_0/D_{50}, smaller anorbital ripples are observed with values of λ that scale with D_{50}. In the WH-94 classification, the ripples transition to sub-orbital ripples for intermediate values of d_0/D_{50}. The WH-94 model is formulated in terms of d_0/η and therefore requires an iterative solution. Malarkey and Davies (2003) present a noniterative solution of WH-94 given as:

$$\begin{aligned}
\lambda_{orb} &= 0.62 d_0 \\
\lambda_{ano} &= 535 D_{50} \\
\lambda_{sub} &= 535 D_{50} \exp\left[-\frac{\log(\lambda_{orb}/\lambda_{ano})\log(0.01 d_0)}{\log(5)}\right] \\
\eta &= \frac{d_0}{\exp\left[B_2 - \sqrt{B_3 - B_1 \log\left(\frac{d_0}{\lambda}\right)}\right]}
\end{aligned} \tag{9}$$

where $B_1 = 10.526$, $B_2 = 7.59$, and $B_3 = 33.6$ and the subscripts indicate orbital, anorbital and suborbital, respectively. Using these values and expressed in terms of external variables, orbital ripples are predicted for $d_0/D_{50} < 1{,}754$, suborbital ripples for $1{,}754 > d_0/D_{50} > 5{,}587$ and anorbitial ripples for $d_0/D_{50} > 5{,}587$.

Models such as WH-94 predict that ripples are in equilibrium with the wave forcing. However, ripples are not active when there is insufficient energy to transport sediment, and as a result the ripples observed under weak wave forcing are usually "relic ripples" left behind from an earlier period of active sediment transport (e.g., Traykovski et al., 1999). Traykovski (2007) demonstrated that the adjustment time of ripples can be longer than the time over which the forcing changes resulting in nonequilibrium ripples even when there is sufficient energy to initiate sediment transport. Detailed imaging of the seabed also highlights that the morphology of ripples is much more complex than the simple orbital and anorbital designations. Hay and Mudge (2005) documented five different bed states that evolved sequentially under increased wave forcing, including irregular ripples, cross ripples, linear transition ripples, lunate megaripples, and flat bed.

While the geometry of the ripples is typically assumed to exert a first order influence on bed roughness, there is limited observational evidence that suggests that z_0 varies as a function of the angle between the current direction and the axis perpendicular to the ripple crest (Θ_{cr}). Drake et al. (1992) found that inferred values of z_0 from logarithmic fits to velocity profiles were significantly reduced when the current was roughly parallel to the ripple crests ($\Theta_{cr} \sim \pm 90°$). These results are supported by laboratory experiments that found reduced bottom roughness estimates for current flows at oblique angles to fix two-dimensional ripples in a flume (Barrantes & Madsen, 2000). Here, we propose a relatively simple model to account for currents at varying angles relative to the ripple crests given as:

$$z_0^{\Theta} = \max\left[a_r \frac{\eta^2}{\lambda} \cos^2\Theta_{cr}, \frac{1}{30} D_{50}\right] \tag{10}$$

where the roughness asymptotes to that based on the Nikuradse roughness for flows parallel to the ripple crests.

3. Methods

3.1. Instrumentation

In order to test the concepts outlined above, a detailed experiment was conducted on the inner continental shelf south of Martha's Vineyard, MA near the MVCO coastal observatory. An instrumented quadpod was deployed for roughly 60 days in two regions of contrasting sediment size and seafloor roughness, but similar depth (Trowbridge et al., 2018). The quadpod supported a suite of instrumentation to measure the currents, turbulence, suspended sediment, vertical density structure and seafloor roughness. In this paper, we will focus our analysis on the data collected by two Nortek Vector acoustic Doppler velocimeter (ADVs) and an Imagenex rotary fan-beam sonar. The sampling volume of each ADV was approximately 0.5 m above the seafloor and the sensors had a horizontal spacing of 1.2 m. The ADVs sampled synchronously at 32 Hz, collecting a 28-minute burst every 2 hours during the first deployment and every hour during the second deployment. The separation between the two ADVs was approximately along-isobath (aligned with the predominant current direction) during the first deployment, and at an angle of approximately 60° with respect to the isobaths during the second.

A rotary sidescan sonar (Imagenex model 881A 1.33 MHz digital tilt-adjusting sonar) provided images of the seafloor with a radius of 5m. The acoustic beam had a 0.8° beam width in azimuth with a 30° spread over the center axis, which was aimed 15° below horizontal. The inner edge of the main beam was at an angle of 45° to the horizontal, resulting in a region with a 1m radius under the sonar with very weak returns. The beam was rotated through 348° in 0.3° increments, with each complete scan of the seafloor taking approximately 2 minutes. Two consecutive 348° scans were conducted every hour. The image resolution is range-dependent and is 1.4 × 2.0 cm 1m from the center of the image and 1.1 × 5.1 cm at the maximum range of 5 m.

Immediately adjacent to the quadpod, a mooring was deployed that measured temperature and salinity 1, 3, 6, 9 and 11m below the mean water surface. Three additional thermistors were deployed on the quadpod at heights 0.24, 1.44 and 2.23m above the seafloor. A conductivity, temperature and depth (CTD) sensor also was deployed on the quadpod 2.1m above the seafloor. Salinity was assumed constant over the range resolved by the thermistors on the quadpod. Both an upward looking 1,000 kHz Nortek acoustic Doppler current profiler (ADCP) and downward looking 2,000 kHz Nortek Aquadopp ADCP were deployed on the

quadpod providing continuous measurements of the current profile above the frame (> 2m above bed) with 0.5m resolution and below the frame (< 1.5m above bed) with 0.2m resolution.

3.2. Analysis

The velocity data from the ADV are rotated into a right-hand coordinate system $x^{\Gamma}=(x_1,x_2,x_3)$, where x_1 is aligned with the mean current and x_3 is the distance above the seafloor. In this coordinate system the mean current is given as $U^{'}=(U_1,U_2,U_3)=(U_c,0,0)$ and the turbulent fluctuations are $u'^{\Gamma}=(u_1',u_2',u_3')$. Thus, in the absence of wave contamination the Reynolds-averaged shear stress is $\langle u'_1u'_3\rangle$, where the angled brackets represent a temporal average over the 28-minute burst. To remove the contamination associated with the sensor orientation in the presence of strong waves, we employ the spatial filtering method proposed by Trowbridge (1998):

$$\langle u_1'u_3'\rangle=\frac{1}{2}\langle\Delta u_1\Delta u_3\rangle \tag{11}$$

where Δu_1 and Δu_3 are the horizontal and vertical velocity calculated by differencing the measurements from the two horizontally separated ADVs. When the horizontal separation between the sensors is large relative to the correlation scale of the turbulence, but small relative to the wavelength of the surface gravity waves, this technique is successful at removing wave contamination (Trowbridge & Elgar, 2001, 2003). More recently, Trowbridge et al. (2018) analyzed the same data we present here, and demonstrate that the observed co-spectra are consistent with a model that accounts for the spectral distortion driven by the advection of turbulence by the wave-induced velocities, providing confidence that this method effectively removes wave motions and provides robust estimates of momentum flux.

In addition to measuring the mean currents and turbulent Reynolds stress, the ADV data are also used to quantify the near bed wave motions. The magnitude of the near bed wave motion, $u_b=\sqrt{\sigma_{u_1}^2+\sigma_{u_2}^2}$, is calculated from the square root of the horizontal velocity variances within the waveband ($0.3<\omega<3\ s^{-1}$). Wave orbital diameter (d_0) is calculated as $d_0=4u_w/\omega$, which is consistent with values of d_0 calculated from significant wave properties and where ω is the radian frequency of the dominant surface waves calculated from the first moment of the velocity spectral components following Madsen et al. (1988).

The orientation of the dominant ripples was determined by rotating each sonar image from its known orientation in earth coordinates to find the angle that maximized the ratio of the acoustic backscatter along the radius of the image from y = 2–5m and x = 0m to the backscatter along the line perpendicular to this radius (y = 3.5m and x = −1.5-1.5m) (Figure 1). After rotation, the backscatter along the line perpendicular to the inferred orientation of the ripple crests was linearly detrended and the start of the ripple shadows was determined from the zero downcrossings. The ripple wavelength λ was calculated as the mean distance between the zero downcrossings along the defined radius. For a sonar mounted near the seafloor,

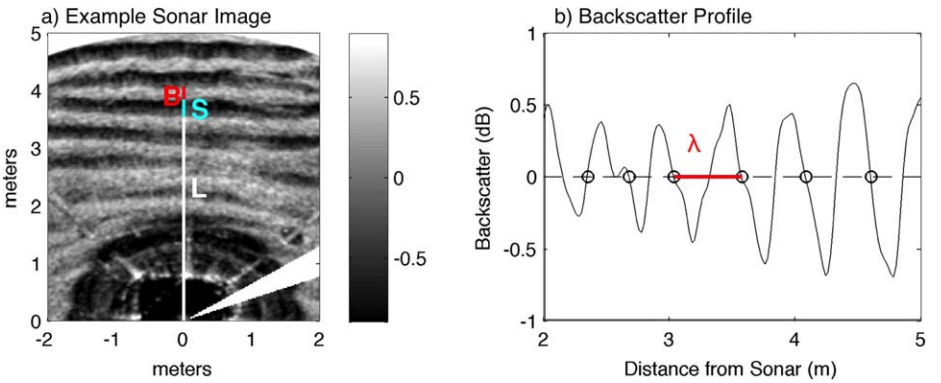

Figure 1. (a) Example of a rotary sidescan image where the variables used in equation (12) are illustrated graphically including the distance from the sonar to the start of a ripple shadow (L), the length of the shadow (S) and the length of the illuminated seabed to the start of the next shadow (B); (b) Amplitude of the acoustic backscatter along the transect perpendicular to the inferred ripple crests, showing the zero crossings (circles) and the associated estimate of the ripple wavelength (λ=B + S)

ripple heights can be estimated from the length and location of the acoustic shadows cast from the bedforms (Jones & Traykovski, 2018). For uniform, symmetric ripples on a flat seabed, η can be estimated from:

$$\eta = \frac{H_i}{2\frac{BL}{S\lambda} + 1} \tag{12}$$

where H_i is the height of the sonar, L is the distance from the sonar to the start of a ripple shadow, S is the length of the shadow and B is the length of the illuminated seabed to the start of the next shadow (see Figure 1, for example). This method provided reasonable estimates of η for the full duration the summer deployment at the coarse site. During the winter deployment at the fine site, the ripples were washed out during energetic wave conditions and the geometric method was not applicable. To estimate ripple height at this site, we use the standard deviation of the sonar backscatter along the line perpendicular to the inferred orientation of the ripples as a proxy for the ripple height. This quantity varies in a manner consistent with the WH-94 prediction for ripple height (see section 4.2), so a simple linear regression between these two quantities was used to convert the standard deviation of the backscatter to η. This estimate of η agrees with the geometric shadow estimate for conditions when ripples are clearly visible on the seafloor. Direct estimates of η based on (12) are preferred because they are based in the known geometry of the sonar and do rely on empirical coefficients derived from an unverified ripple model.

3.3. Data Quality Criteria

Direct covariance momentum flux measurements require high quality velocity data that resolve turbulent fluctuations. There are a number of potential sources of error, including electronic noise, sensor fouling/interference and low signal-to-noise ratios for acoustic sensors. To identify spurious velocity data, all values with a reported velocity correlation below 80% or where the magnitude of the velocity was more than 7 standard deviations above the burst mean, are flagged as bad. These bad data are replaced with values equal to the burst mean, and all bursts with more than 10% bad data are excluded from further analysis. During the first deployment (summer) there was an unidentified source of electronic noise that resulted in a relatively large amount of bad data, with 41.4% of the bursts excluded based on this criterion. During the second deployment, the source of noise was largely absent resulting in the exclusion of only 4% of the bursts.

It is also important to assess whether the simple differencing method that is used, effectively removes contamination by waves. This was done by comparing the observed co-spectra of the differenced velocities (equation (11)) to the model proposed by Trowbridge et al. (2018), which accounts for the distortion of the cospectra by wave advection. All bursts where the rms error between the observed cospectra and the model is greater than 0.5 also are excluded from the analysis. This resulted in the exclusion of another 6.5% and 11.3% of the bursts from the summer and winter deployments, respectively. Finally, all bursts where $C_d < 0$ or $C_d > 0.02$ also are excluded (1.4% for summer and 2.7% for winter). Using these criteria, ~51% and ~82% of the bursts are included in our analysis from the summer and winter deployments, respectively.

4. Results

4.1. Overview of Experiments

The data analyzed below were collected from the inner continental shelf south of Martha's Vineyard, MA (see also, Trowbridge et al., 2018). This region is characterized by sorted bedforms or ripple-scour depressions (RSDs) (Goff et al., 2005), which result in alternating swaths of coarse and fine sand that support contrasting types of wave-induced ripples. The quadpod frame was deployed from mid July to late August and then again from mid November to late December in 2014. The summer deployment was within a RSD where a grab sample with a median grain size of 780 μm was collected and large orbital ripples are observed. The winter deployment was immediately to the east of the RSD in an area of fine sand where sub-orbital ripples are observed. No grab sample was collected at the fine site, but a sample collected at a nearby location outside of the RSD had a D_{50} of 170 μm. The mean water depth at the coarse and fine sites is 16.2m and 17.9m, respectively.

The summer deployment is characterized by weak to moderate winds (<10 m/s) from the southwest, with the exception of strong winds from the north associated with the passage of Tropical Storm Arthur on 4–5 July 2014 (Figure 2a). Waves during the summer exceed 1.5m less than 10 percent of the deployment and

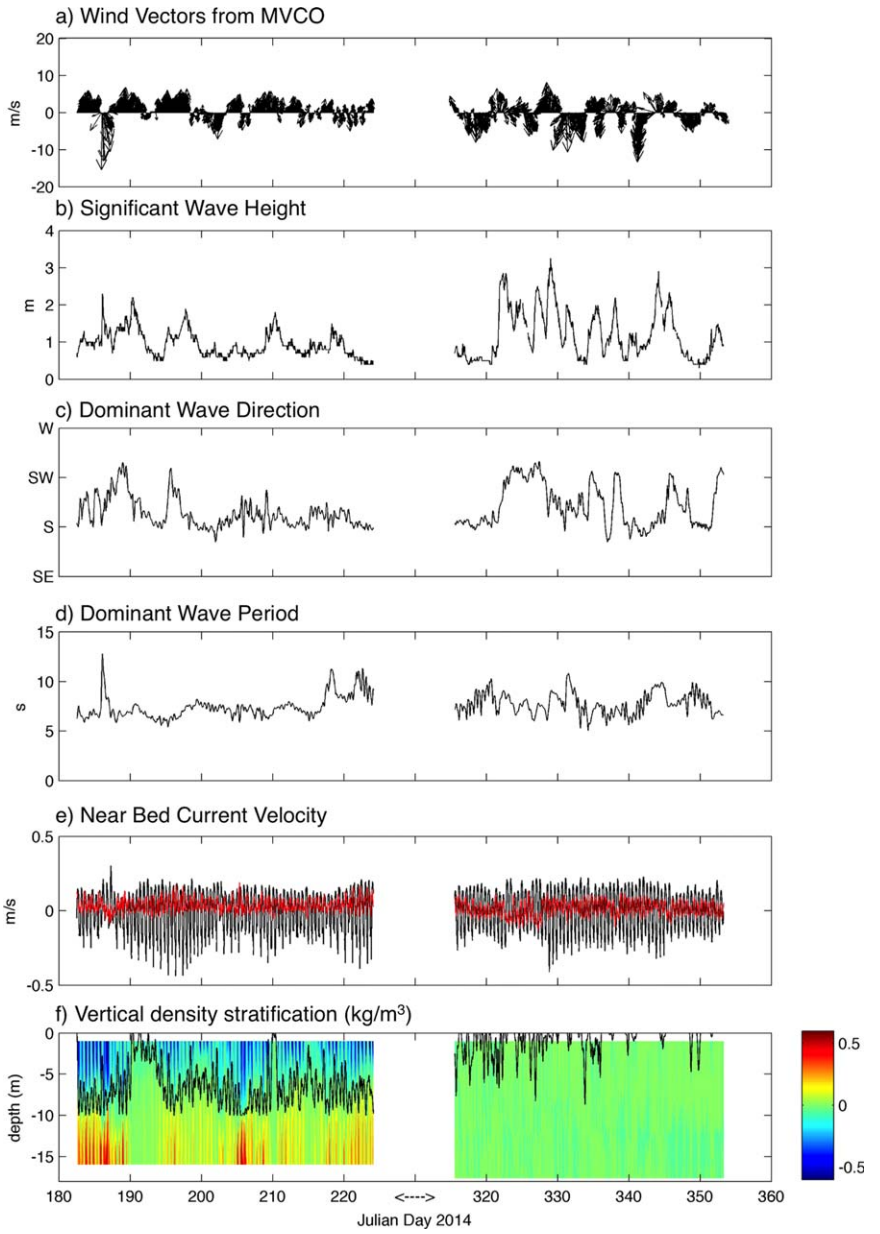

Figure 2. (a) Wind speed vectors measured at the MVCO Air-Sea Interaction tower; (b) Significant wave height measured at MVCO node; (c) dominant wave direction from near-bed wave velocities; (d) dominant wave period from near-bed wave velocities; (e) Near-bed currents measured ~0.5m above the seafloor including along shelf (black, positive toward east) and across shelf (red, positive toward north); (f) Contours of the density anomaly (deviation from depth mean) from CTD data on mooring and quadpod, including the height of the bottom boundary layer (black line), estimated from the location closest to the bed where the gradient Richardson number is greater than 0.25. Note, x-axis is discontinuous.

never exceed 2.5m (Figure 2b). The average wave period is ~6s and the dominant wave direction is from the S/SW, consistent with locally generated seas (Figures 2c and 2d). During the winter deployment, the winds are more energetic with frequent winds from the N/NW associated with the passage of cold fronts. The waves exceed 1.5m roughly 30 percent of the deployment and the maximum observed wave height is ~ 3m. Elevated waves are generally associated with strong winds from the S/SW resulting in predominantly locally-generated wind waves. The near-bed currents are dominated by the M2-tide, which is primarily directed along-shelf with a maximum near-bed velocity of ~ 0.4 m/s (Figure 2e). Burst-averaged vertical velocities (data not shown) were nearly 2 orders of magnitude smaller than the horizontal velocities,

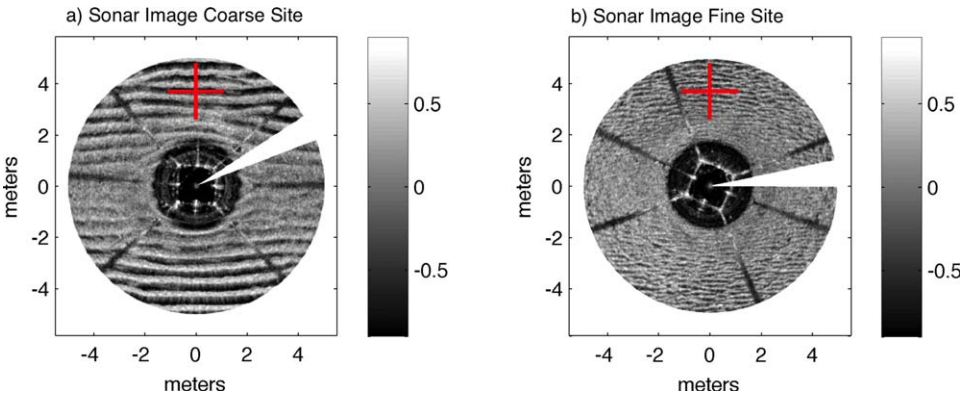

Figure 3. Examples of the rotary sonar data showing (a) the orbital ripples that characterize the coarse site, and (b) the irregular sub-orbital ripples that characterized the fine site. Both images have been rotated so that the inferred orientation of the ripple crests is perpendicular to vertical. The rotation was determined by maximizing the ratio of the acoustic backscatter along the vertical and horizontal lines shown in red.

suggesting that boundary layer ventilation resulting from a permeable seabed (Conley & Inman, 1994) did not significantly impact the turbulence measured by our sensors.

The summer deployment was characterized by measureable density stratification that was almost exclusively controlled by the vertical temperature structure (Figure 2f). The winter deployment as mostly well-mixed with little to no vertical density gradients resolved by the moored instruments. The thickness of the bottom boundary layer (δ_c) was estimated by calculating the height closest to the bottom where the gradient Richardson number exceeded 0.25. During the summer deployment, the bottom boundary layer was often only a fraction of the total water depth (Figure 2f). However, during both the summer and winter deployments the boundary layer thickness was always greater than ten times the height of the ADV sampling above the bottom, consistent with the assumption that the measurements fall within the constant stress portion of the boundary layer ($z > 0.1\ \delta_c$).

4.2. Variations in Bed Roughness

Sonar images from the coarse site during the summer deployment reveal large orbital ripples (Figure 3a) with wavelengths between 0.4-0.8m (Figures 4 and 5). During conditions when $u_b > 0.14$ m/s, the ripples are active, and changes in both ripple orientation and wavelength are observed (Figures 4 and 5). Conditions when $u_b > 0.14$ m/s represent less than 10% of the summer deployment, and outside of these energetic wave conditions the ripple orientation and wavelength remain essentially constant, consistent with relic features not in equilibrium with the wave forcing. This nonequilibrium behavior is clearly seen by comparing the observed ripple wavelength to the WH-94 equilibrium model (Figure 5). During energetic wave conditions the adjustment of the ripple wavelength lags the forcing, and as the wave forcing wanes, the wavelength stops adjusting leaving behind ripples with wavelengths significantly longer than the equilibrium wave conditions would dictate, consistent with the results of Traykovski (2007).

Similar to the observed changes in ripple wavelength, the largest changes in ripple height also occur during strong wave forcing (Figure 5). During most of the wave events, the ripple heights initially decrease before rapidly increasing. The ripple height also lags the equilibrium prediction, never reaching the maximum value predicted at the peak of the wave event. During the waning phase of wave events, the ripple height generally decreases. Between wave events, the ripple heights continue to decrease unlike the ripple wavelength and orientation, which both remain virtually unchanged in between events. It is unlikely that this decrease in η is an adjustment to the wave forcing and most likely represents degradation of the wave-formed ripples by either the mean currents or biological processes (e.g., Hay, 2008).

Despite the clear nonequilibrium behavior of the ripples at this site, the simple equilibrium orbital ripple model of WH-94 (equation (9)) does a reasonable job capturing the time variations in the observed bed roughness ($r = 0.74$). The values of z_0^{rip} inferred from the ripple shadows in conjunction with equation (8) are generally smaller than predicted by the equilibrium model, largely because the relict ripple wavelengths are often much larger than the equilibrium prediction under weak wave conditions. Significant differences

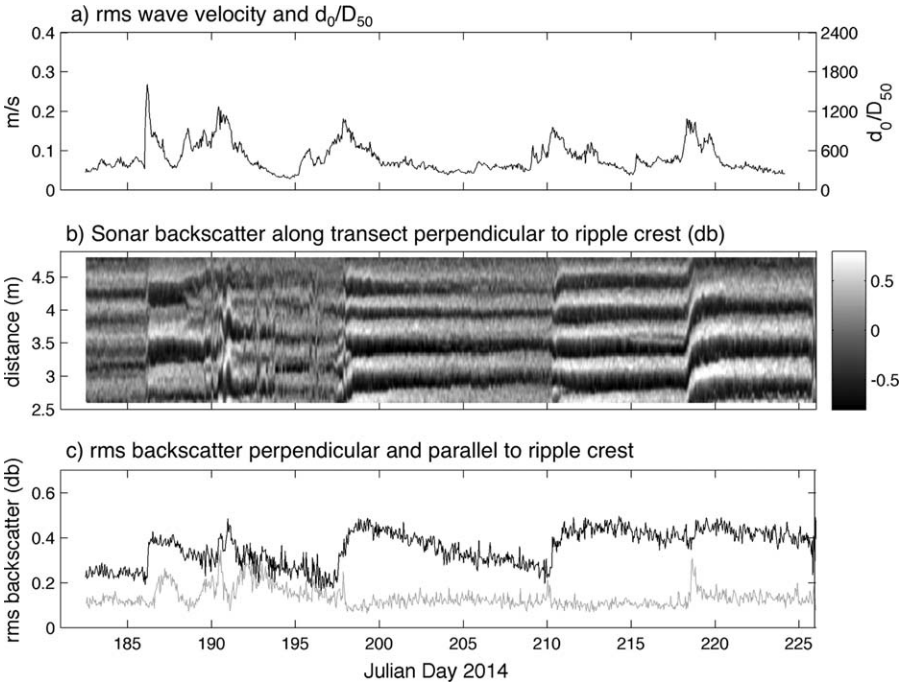

Figure 4. Temporal variability of the ripples observed at the coarse site as a function of wave energy including (a) the rms wave velocity (left axis) and d_0/D_{50} (right axis) calculated using the deployment mean wave period; (b) acoustic backscatter from a transect perpendicular to the ripple crests; c) rms of the acoustic backscatter perpendicular to the ripple crests (black line) and parallel to ripple crests (gray line). The 2-D orbital ripples at this site only adjust under energetic wave forcing leaving behind relic ripples whose amplitude decays with time and are anisotropic at the scales resolved by the sonar.

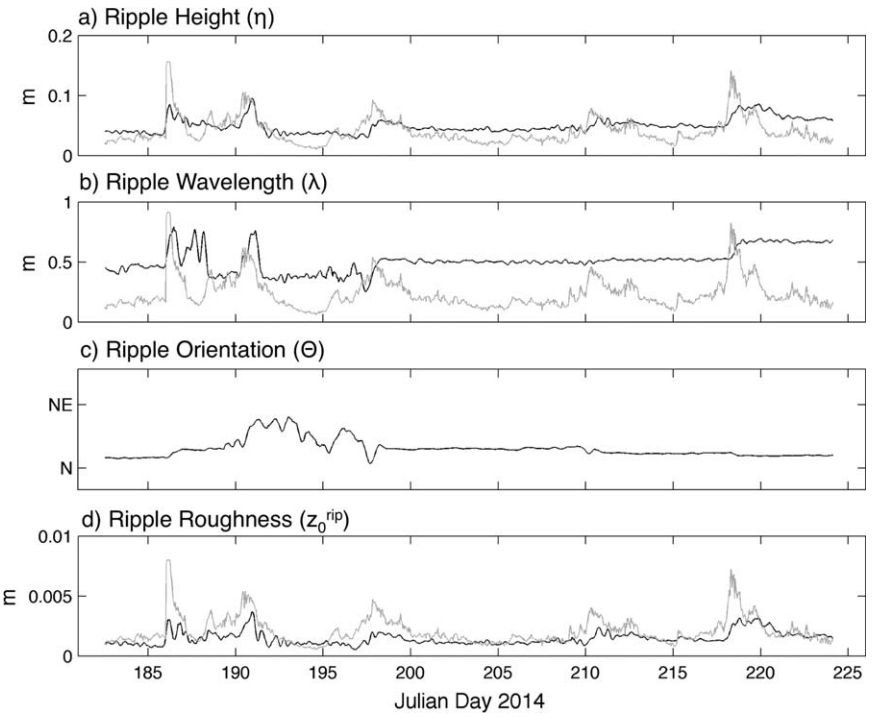

Figure 5. Estimates of the ripple geometry from the coarse site including (a) ripple height (η); (b) ripple wavelength (λ); (c) ripple orientation measured as the angle perpendicular to the ripple crests (Θ); and d) ripple roughness ($z_0^{rip} = a_r\eta^2/\lambda$). In Figures 5a, 5b, and 5d the black line represents the measured values from the sonar images and the gray line represents the prediction from the Wiberg and Harris (1994) model.

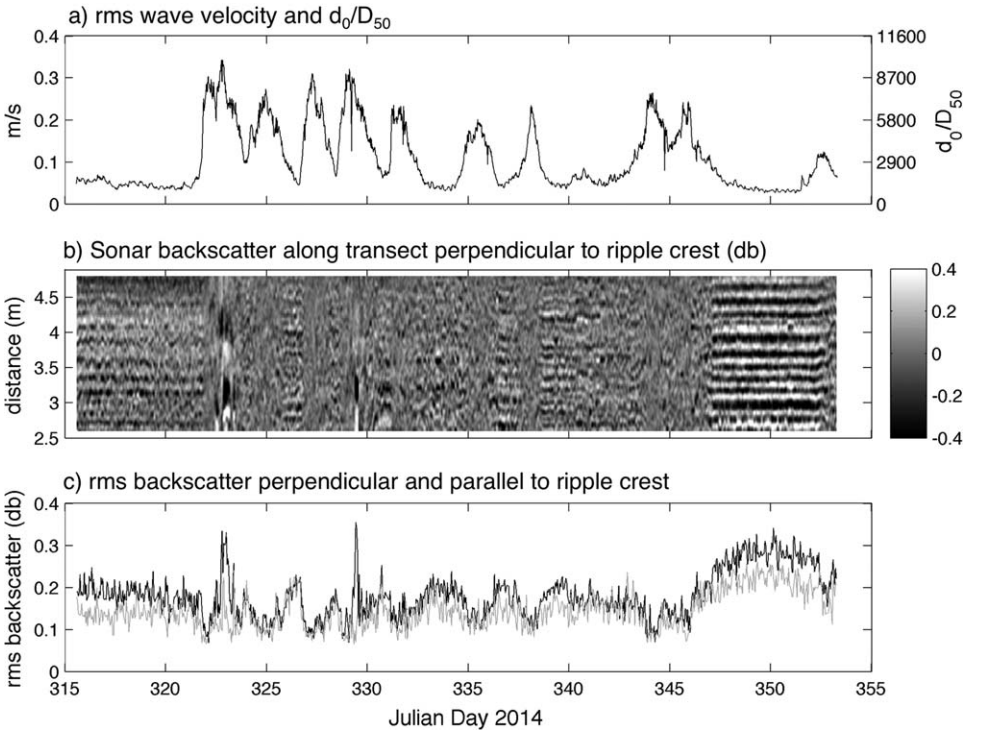

Figure 6. Temporal variability of the ripples observed at the fine site as a function of wave energy including (a) the rms wave velocity (left axis) and d_0/D_{50} (right axis) calculated using the deployment mean wave period; (b) acoustic backscatter from a transect perpendicular to the ripple crests; (c) rms of the acoustic backscatter perpendicular to the ripple crests (black line) and parallel to ripple crests (gray line). The 3-D sub-orbital ripples at this site are washed out during energetic waves conditions and the roughness is only slightly anisotropic, as suggested by the ratio of the backscatter perpendicular to the backscatter parallel to the ripple crest.

between the model and inferred bed roughness also occur during the early stages of wave events when the nonequilibrium adjustment of the ripple height results in a significantly lower value of z_0^{rip} than predicted by the equilibrium model (Figure 5).

At the fine site during the winter deployment and under weak wave forcing, the observed ripples have smaller wavelengths ($\sim$0.2m) consistent with "sub-orbital" ripples and are similar in appearance to the "irregular ripples" described by Hay and Mudge (2005) (Figure 6). Easily identifiable ripples are only obvious in the sonar data during low wave conditions ($u_b < 0.10$ m/s), when the ripple wavelength remains relatively constant and large changes in orientation are not observed (Figure 7). When $u_b > 0.3$ m/s, no ripples are visible and the bed is essentially flat. For intermediate wave conditions, the bed is more complex with a variety of length scales apparent. As a result, the estimate of ripple wavelength from the sonar data increases during some of the wave events, but in reality no ripples are clearly visible during these conditions. The WH-94 model predicts that ripple wavelengths decrease during significant wave events, with the sub-orbital ripples transitioning to shorter anorbital ripples when $d_0/D_{50} > 5{,}600$. There is evidence in the sonar data that anorbital ripples with wavelengths $\sim$ 0.10m are formed under strong wave forcing (Figure 8). We interpret these ripples as the "linear-transition ripples" described by Hay and Mudge (2005); however they are superimposed on irregular larger scale features on the seabed, perhaps the early development of lunate megaripples (Figure 8). Our data do not clearly exhibit all of the bed states identified by Hay and Mudge (2005), presumably because the forcing changes so rapidly that the intermediate morphologies do not have time to develop. As a result, most of our data are consistent with either "irregular ripples" under weak waves or a flat bed under strong waves.

Under conditions of strong wave forcing, the standard deviation of the backscatter perpendicular to the inferred ripple crests goes down significantly (Figure 6). This behavior is consistent with the WH-94 model that predicts that ripple heights decrease with increasing wave forcing (i.e., d_0/D_{50}) when suborbital and

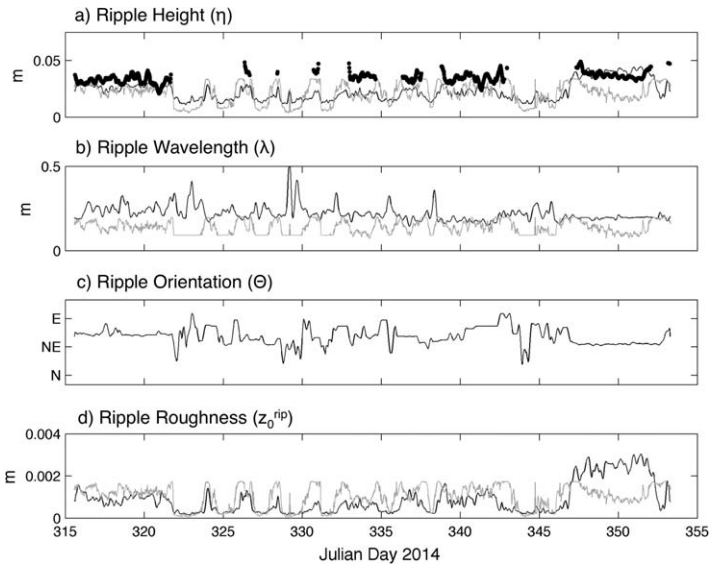

Figure 7. Estimates of the ripple geometry from the fine site including (a) ripple height (η); (b) ripple wavelength (λ); (c) ripple orientation measured as the angle perpendicular to the ripple crests (Θ); and d) ripple roughness ($z_0^{rip} = a_r\eta^2/\lambda$). In a), b) and d) the black line represents the measured values from the sonar images and the gray line represents the prediction from the Wiberg and Harris (1994) model. In panel a) the black dots represent the estimates of ripple height from the shadow geometry for conditions when clear ripples are present in the sonar images.

anorbital ripples are present. With the exception of the last 7 days of the deployment, the correlation between the standard deviation of the sonar backscatter and the ripple height predicted by the WH-94 model is good (r = 0.73) and the estimates of η agree favorably with the estimates from the sonar shadows (equation (9)) when clear ripples are observed (Figure 7). The inferred values of z_0^{rip} from the sonar data and equation (5) are largely consistent with the prediction of the WH-94. The most notable differences occur over the last 7 days of the deployment, when the inferred roughness exceeds the ripple model prediction by roughly a factor of three.

In addition to the obvious differences in the types of ripples present at the coarse and fine sites, the sonar data illustrate other important differences between the two locations. At the coarse site, the inferred ripple height is positively correlated with wave forcing suggesting that bed roughness increases with increasing wave energy. At the fine site, the inferred ripple height decreases with wave energy and the estimates of bed roughness decrease by roughly an order of magnitude during strong wave events. At the coarse site, the ripple crests are oriented nearly parallel to the local bathymetry, whereas the smaller ripples at the fine site are oriented at a significant angle to the bathymetry (Figures 5c and 7c). The data also suggest that the smaller ripples at the fine site are much more 3-dimensional at the scales resolved by the sonar. At the coarse site, the orientation of the larger orbital ripples is relatively easy to determine and the standard deviation of the backscatter perpendicular to the ripple crests is generally more than twice the standard deviation of the backscatter parallel to ripple crests (Figure 4c). In contrast, determining the exact orientation of the ripples at the fine site is more challenging and even during low wave conditions, when the sub-orbital ripples are relatively clear, the standard deviation of the backscatter perpendicular to the ripple crests is seldom more than 50% greater than in the direction parallel to ripple crests, consistent with more isotropic roughness (Figure 6c).

4.3. Variations in Drag Coefficient

Given the differences in wave forcing and the type and response of the observed ripples, we expect significant differences in the magnitude and variations of the drag coefficient inferred from the Reynolds stress estimates at the two sites. During the summer deployment at the coarse site, C_d varies by over an order of magnitude (Figure 9), with maximum values exceeding 0.01 and minimum values that are less than a simple estimate based solely on the grain roughness (equation (3), with $z_0 = D_{50}/30$). The fine site also exhibits significant variability, however the standard deviation in C_d is 50% smaller than at the coarse location

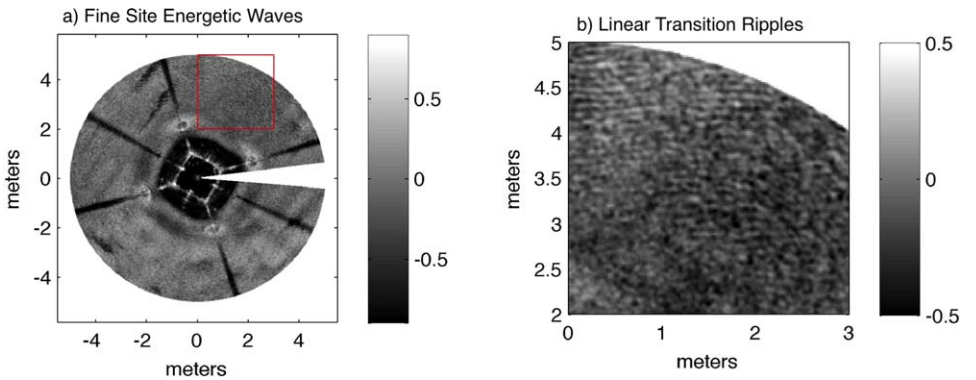

Figure 8. Example of the rotary sonar data from the fine site under energetic forcing. The sub-orbital ripples are washed out and the seafloor is characterized by heterogeneous large scale features seen in Figure 8a with superimposed linear-transition ripples seen in Figure 8b. The red box in panel a) shows the region of detail shown in panel b).

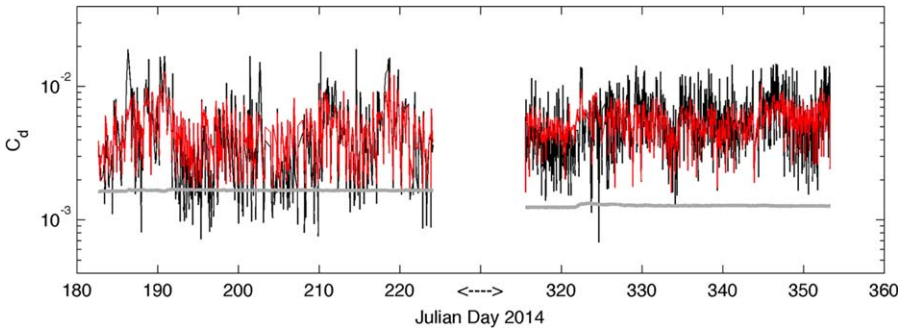

Figure 9. Variations in the drag coefficient (C_d) during both the summer (coarse) and winter (fine) deployments. The black line is the drag coefficient inferred from the observed Reynolds stress and the red line is the estimated drag coefficient from the Grant & Madsen model using the measured bed roughness (z_0^{Θ}) and accounting for the orientation of the current relative to the ripple crests (Θ_{cr}). The thick gray line is the hydraulically rough value of the drag coefficient associated only with the grain roughness (equation (3), with $z_0 = D_{50}/30$). Note that the x-axis is discontinuous and values of C_d are plotted as a line even though the data are discontinuous (e.g., bad data are omitted).

(Figure 9). During both deployments, estimates of C_d generally increase with increasing wave forcing. At the fine site, this increase in C_d is inconsistent with the estimates of bed roughness, which were inferred to decrease under strong wave forcing (Figure 7).

In order to quantify the importance of variations in bed roughness and wave-current interaction, the direct estimates of C_d are compared with four models of varying complexity (Figures 10 and 11; Table 1). The first model (denoted $C_d^{z_0}$) uses the estimates of z_0^{rip} (equation (8)) inferred from the sonar data, but does not

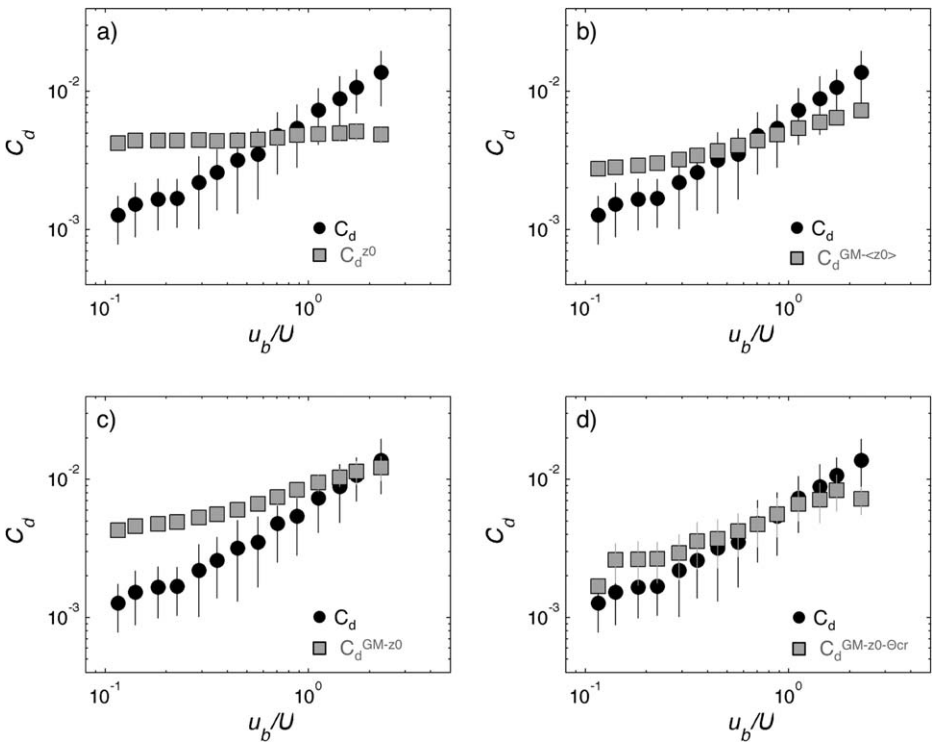

Figure 10. Data from the coarse site showing the variations in drag coefficient as a function of the ratio of the near bed wave (u_b) to mean current (U) velocity. The inferred values of the drag coefficient based on the measured Reynolds stress (black circles) are compared to estimates of the drag coefficient (gray squares) calculate from: (a) only the observed bed roughness (C_d^{z0}); (b) GM-79 using a constant value for z_0 ($C_d^{GM-<z0>}$); (c) GM-79 using the observed z_0 (C_d^{GM-z0}); and (d) GM-79 using the observed z_0 and accounting for the orientation of the current relative to the ripples ($C_d^{GM-z0-\Theta cr}$). The data have been bin-averaged as a function of u_b/U and the vertical lines indicate ± 1 standard deviation.

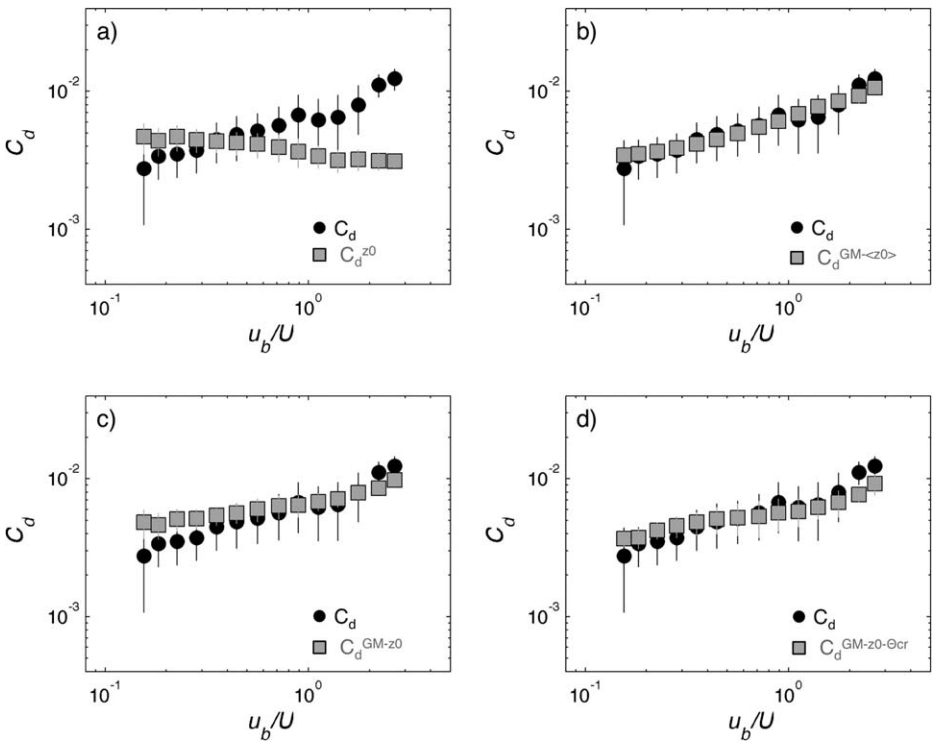

Figure 11. Same as figure 10, but for fine site.

account for wave-current interaction. The second model (denoted $C_d^{GM-\langle z_0\rangle}$) applies the wave-current model of GM-79, but utilizes a constant value of z_0 selected so that the deployment-averaged value of C_d is equal to the observed deployment mean. The third model (denoted $C_d^{GM-z_0}$) applies the wave-current model of GM-79 and the time-varying bed roughness estimates inferred from the sonar data (equation (8)). The final model (denoted $C_d^{GM-z_0-\Theta_{cr}}$) includes wave-current interaction and the roughness inferred from the sonar data accounting for the angle of the current relative to the inferred ripple crests (z_0^{Θ}) via equation (10). We used a value of $a_r = 0.3$ to calculate both z_0^{rip} and z_0^{Θ}. This is at the low end of the values suggested by Soulsby (1997), but provided the best overall agreement with our estimates of C_d.

At the coarse site, the measured values of C_d are positively correlated with $C_d^{z_0}$, consistent with positive relationship between u_b and z_0^{rip} seen at this location, but $C_d^{z_0}$ fails to capture the majority of the observed variability in C_d, particularly as a function of u_b/U (Figure 10). Values of $C_d^{GM-\langle z_0\rangle}$ have much higher skill and are

Table 1
Definition of the Models of Drag Coefficient and Comparison of Their Correlation Coefficient (r) and Brier Skill Score With the Observed Drag Coefficient

	Model			
	$C_d^{z_0}$	$C_d^{GM-\langle z_0\rangle}$	$C_d^{GM-z_0}$	$C_d^{GM-z_0-\Theta_{cr}}$
Wave-current interaction?	No	GM-79	GM-79	GM-79
z_0	Equation (8)	Constant	Equation (8)	Equation (10)
Coarse site				
Correlation	0.43	0.77	0.75	0.79
Brier Skill	0.11	0.37	0.55	0.60
Fine Site				
Correlation	−0.09	0.50	0.51	0.53
Brier Skill	−0.21	0.24	0.26	0.28

Note. Both the correlation and brier skill score are calculated for the discrete observations (no bin averaging).

more strongly correlated with the observations, but fail to capture the full range of the observed values of C_d, particularly the lower observed values under weak wave forcing. Including the roughness inferred from the sonar along with wave-current interaction does result in moderate improvement in skill, but this model still does not capture the full variability inferred from the data. The only model that begins to capture the full variability of the observed values of C_d is the model that takes into account the orientation of the current relative to the observed ripples (Figure 10d). At the coarse site, this model has the highest overall skill and exhibits the strongest correlation with the observed values of C_d (Table 1).

At the fine site, the model with the highest skill and strongest correlation with the data is the full model that includes wave-current interaction, the bed roughness inferred from the sonar data and the angle of the current relative to the observed ripples ($C_d^{GM-z_0-\Theta_{cr}}$). The model that accounts for the observed bed roughness but not wave-current interaction ($C_d^{z_0}$) is negatively correlated with the data and has negative skill (Table 1). This occurs at the fine site because the inferred drag increases during strong wave events, conditions when the bed roughness is observed to decrease in the sonar data. The observed increase in C_d during increased wave forcing is consistent with wave-current interaction and accounting for this via the GM-79 model increases both the model skill and correlation with the data at the fine site. Including the roughness inferred from the sonar data and wave-current interaction ($C_d^{GM-z_0}$) results in essentially no change in skill or correlation as compared to the model with a constant value of z_0 ($C_d^{GM-\langle z_0\rangle}$). Similarly, while the best agreement with the data comes from the full model that includes the orientation of ripples relative to the current, the improvements relative to $C_d^{GM-z_0}$ and $C_d^{GM-\langle z_0\rangle}$ are modest at the fine site (Table 1).

The variations in C_d based on the observed Reynolds stress at both sites highlight the importance of wave-current interaction in enhancing the frictional resistance of the overlying flow. The GM-79 model reasonably captures the observed variability at both sites, when the appropriate bed roughness is known. At the coarse site, where the large 2-D orbital ripples are observed, it is important to capture not only the wave-current interaction, but also the observed bed roughness and the orientation of the current relative to the ripples. While the roughness inferred from the sonar generally increases with increased wave forcing, this is clearly not the main factor that causes the large increase in C_d as a function of u_b/U (Figure 10a). Including wave-current interaction does increase the variability, but the order of magnitude increase in C_d as a function of u_b/U is only captured when the relative angle between the current and ripples is accounted for (Figure 10d). At the fine site, the observed variability of C_d as a function of u_b/U is weaker (Figure 11).

It should be noted that Θ_{cr} and u_b/U are not independent. The strongest tidal flows (and hence lower values of u_b/U) are directed primarily along along-shelf, which at the coarse site corresponds to flows that are mostly parallel to the inferred ripple crests. The slight rotary nature of the tides at this location results in weak tidal flows (and hence higher values of u_b/U) that are directed on/off shore, or more perpendicular to the ripple crests. At the fine site, when ripples are clearly visible in the sonar, they are oriented at a much larger angle relative to the bathymetry (Figure 7c) and the covariance between Θ_{cr} and u_b/U is weaker. As a result, C_d varies much more at the coarse site when averaged as a function of u_b/U than at the fine site. Thus, a significant fraction of the variability at the coarse site results from Θ_{cr}, which is correlated with u_b/U. At the fine site, not only does C_d vary more weakly when averaged as a function of u_b/U, but the variability in C_d as a function of u_b/U is well captured by a constant value of z_0 ($C_d^{GM-\langle z_0\rangle}$).

5. Discussion

There are several notable differences between the drag coefficients observed at the coarse and fine sites. First, the average value of C_d measured at the coarse site (0.0043 $\pm$0.0037) is 20% smaller than at the fine site (0.0052 $\pm$0.0024) despite the presence of large orbital ripples at the coarse site and smaller sub-orbital ripples at the fine site. The average sonar estimate of z_0^{rip} at the coarse site ($z_0^{rip} \sim 1.4 \times 10^{-3}$ m) is roughly 45% larger than the average estimate from the fine site ($z_0^{rip} \sim 1.0 \times 10^{-3}$ m). The deployment at the fine site took place during the winter and had more energetic waves than the summer deployment (coarse site), so the greater value of C_d could reflect enhanced wave-current interaction. However, under strong wave forcing ($u_b/U > 1$) average values of C_d are greater at the coarse site than the fine site (Figures 10 and 11) and conditions when C_d is larger at the fine site generally correspond to lower wave conditions ($u_b/U < 1$). Trembanis et al. (2004) found similar results under nonstorm conditions, with slightly larger roughness over a site with small ripples than at an adjacent site with large orbital ripples. The inferred orientation of the

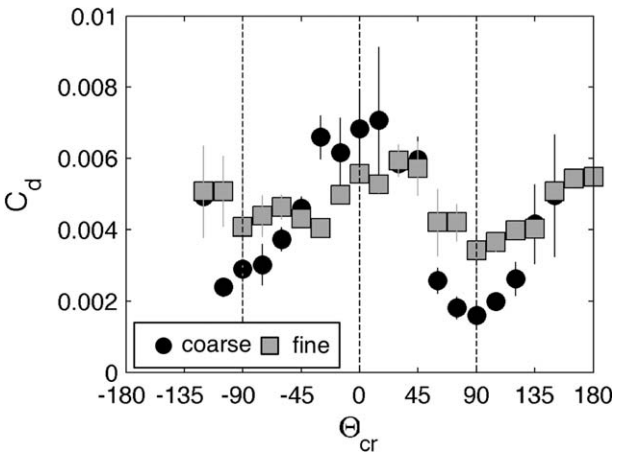

Figure 12. Values of the measured drag coefficient for the coarse (black circles) and fine (gray squares) sites bin-averaged as a function of the angle between the mean current direction and the direction perpendicular to the inferred ripple crests (Θ_{cr}). Vertical lines represent ± 1 standard error. Both sites show a dependence on Θ_{cr}, with greater sensitivity at the coarse site where the estimates of C_d are more than a factor of 4 smaller when the current is parallel to the ripple crests ($\Theta_{cr} \sim \pm 90°$).

large orbital ripple crests at the coarse site is largely parallel to shore and aligned with the direction of the dominant tidal currents (Figure 5c). In contrast, the inferred orientation of smaller sub-orbital ripple crests at the fine site is at a significant angle to the shoreline and hence the dominant along-shore tidal currents (Figure 7c). After accounting for the orientation of the ripples relative to the current following equation (10) the mean roughness estimate from the sonar shadows at the coarse site (3.9×10^{-4} m) is significantly smaller than the mean roughness at the fine site (6.2×10^{-4} m).

Values of C_d exhibit a greater sensitivity to Θ_{cr} at the coarse site than at the fine site (Figure 12). Bin-averaged values of C_d as a function of Θ_{cr} vary by more than a factor of 4 at the coarse site, but less than a factor of 2 at the fine site. Values of C_d at the coarse site are larger than the values at the fine site when the current is roughly perpendicular to the inferred orientation of the ripple crests ($\Theta_{cr} \sim 0°$) but when the flow is parallel to the ripple crests ($\Theta_{cr} \sim \pm 90°$) the values of C_d at the coarse site drop well below those at the fine site (Figure 12). We hypothesize that the greater sensitivity to Θ_{cr} at the coarse results from the large 2-dimensional orbital ripples at this location. At the coarse site, the standard deviation of the sonar backscatter in the direction perpendicular to the ripple crests is more than twice the backscatter parallel to the ripple crests (Figure 4c). In contrast, the smaller sub-orbital ripples at the fine side are observed to be more 3-dimensional with more isotropic backscatter in the sonar images. It is also worth noting that because determining the ripple orientation at the fine site is much more difficult than at the coarse site our estimates of Θ_{cr} are much less precise, particularly under strong wave forcing, for the smaller sub-orbital ripples.

Given the uncertainties in our estimates of z_0 from the sonar data, it is instructive to infer the apparent roughness from our observations. To avoid the known issues associated with fitting a logarithmic velocity profile (Grant & Madsen, 1986; Gross et al., 1992), we infer z_0 by finding the value that minimizes the least squares error between our covariance estimate of stress and the predicted stress from GM-79. While the estimates of z_0 from this method (denoted z_0^{fit}) are noisy, they generally support our inferences about the seafloor from the sonar data. Values of z_0^{fit} increase with elevated wave forcing at the coarse site and decrease with elevated wave forcing at the fine site (data not shown). At both sites, z_0^{fit} shows a dependence on Θ_{cr}, with the largest values for conditions when the current is perpendicular to the inferred orientation of the ripple crests ($\Theta_{cr} = 0$) (Figure 13). At the coarse site, values of z_0^{fit} vary by more than 2 orders of

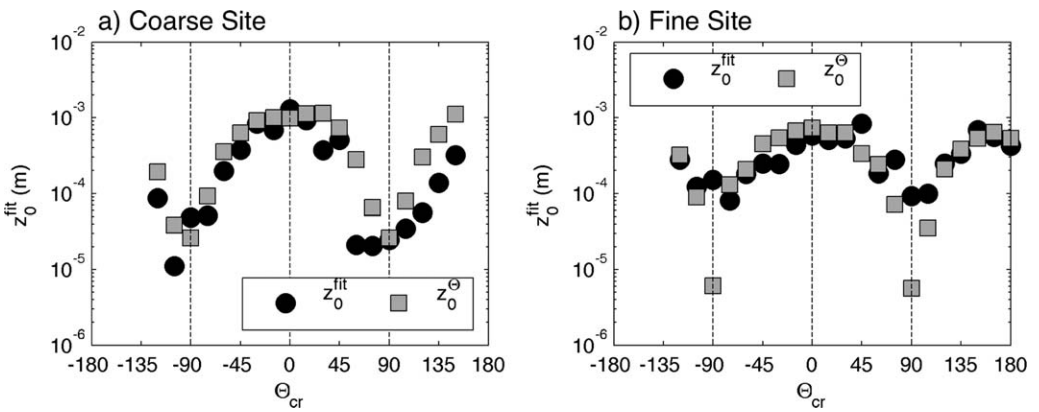

Figure 13. Values of z_0^{fit} inferred by minimizing the least squares error between the observed stress and the stress predicted by the GM-79 model at (a) the course site and (b) the fine site. Values of z_0^{fit} (black circles) are compared to sonar estimates of z_0^{Θ} (gray squares) accounting for the angle between the mean current and ripple orientation (equation (10)). The data have been bin-averaged as a function of Θ_{cr}.

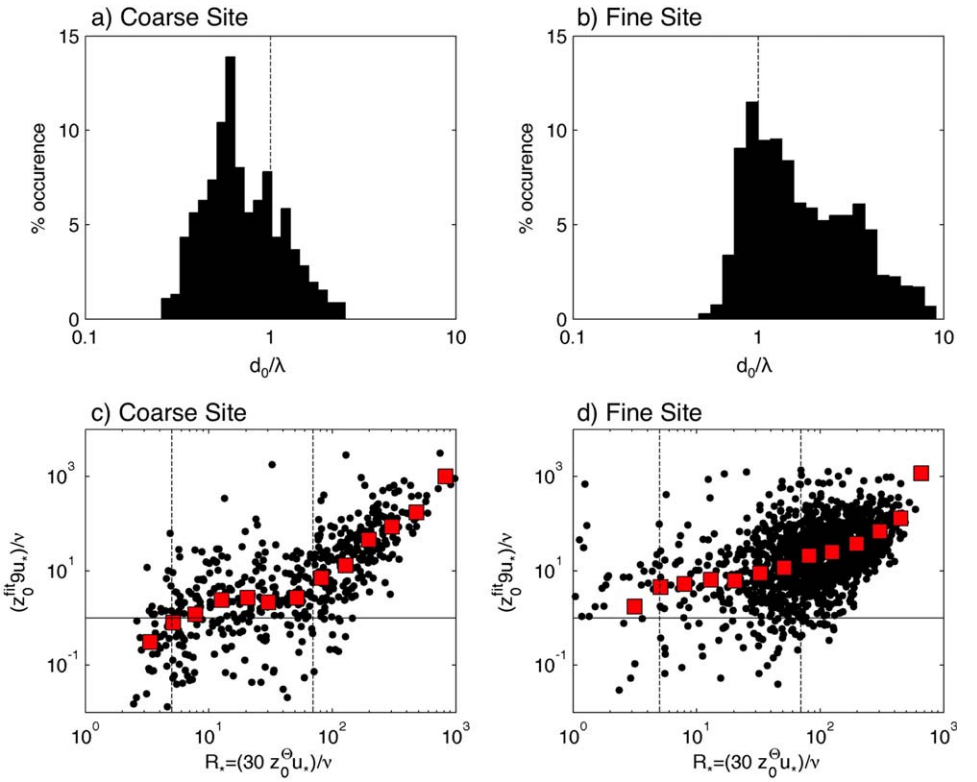

Figure 14. Histograms of the ratio of the wave orbital excursion (d_0) to the ripple wavelength (λ) for (a) the coarse site and (b) the fine site and comparison of the modeled z_0^{Θ} (equation 10) to the inferred values of roughness inferred by minimizing the least squares error between the observed stress and the stress predicted by the GM-79 model (z_0^{fit}) for c) the coarse site and d) the fine site. The modeled values of z_0 are nondimensionalized to be consistent with the boundary Reynolds number (R_*) and z_0^{fit} is nondimensionalized by the hydraulically smooth value (e.g., $9u_*/\nu$). Black dots represent the individual data points and the red squares are bin-averaged values. The data asymptote toward the hydraulically smooth value when $R_*<70$ at the coarse site, where the majority of the data have $d_0/\lambda < 1$, but remain above the hydraulically smooth value at the fine site where $d_0/\lambda > 1$.

magnitude as a function of Θ_{cr} and this variability is well captured by z_0^{Θ}. At the fine site, values of z_0^{fit} show an order of magnitude less variability with respect to Θ_{cr}. As a result, the proposed z_0^{Θ} formulation significantly over-predicts the variability of the inferred roughness as a function of Θ_{cr}, and on average the observed value of z_0^{Θ} is much smaller than z_0^{fit} when $\Theta_{cr} = \pm 90°$, consistent with the more isotropic roughness inferred at this site.

As seen in Figure 9, values of C_d at the coarse site are less than the value associated with the grain roughness (equation (3)) roughly 15% of the time. The low values of C_d typically occur during low wave conditions when the flow is roughly parallel to the large orbital ripples that are not in equilibrium with the wave forcing ($\lambda > d_0$) (Figure 14a). For these conditions, we assume that neither the currents nor the waves experience the roughness associated with ripples and that the roughness scale is set by the bed sediment ($k_s \sim D_{50}$). Under these conditions, our observations suggest that the flow at the coarse site may not be hydraulically rough ($R_* < 70$). This hypothesis is supported if we calculate R_* assuming that equation (10) reasonably represents the appropriate bed roughness length ($k_s \sim 30z_0$). At values of $R_* > 70$, the values of z_0^{fit} are much larger than the hydraulically smooth value ($z_0 \sim \nu/(9u_{*c})$) and increase with increasing R_* at the coarse site (Figure 14c). However, as R_* drops below 70, z_0^{fit} asymptotically approaches the hydraulically smooth estimate. There is considerable scatter in this relationship, but most of the values where $z_0 \sim \nu/(9u_{*c})$ occur when $R_* < 70$. Additionally, these conditions also occur when relic ripples are present, suggesting that the flow is no longer hydraulically rough when both $R_* < 70$ and $\lambda > d_0$.

In contrast to the coarse site, estimates of C_d essentially never fall below the value associated with the grain roughness at the fine site (Figure 9). Values of z_0^{fit} generally are much larger than $\nu/(9u_{*c})$, even when

$R_* < 70$ (Figure 14d). At the fine site, the ripples are much smaller and the orbital diameter is nearly always larger than the ripple wavelength ($d_0 > \lambda$) (Figure 14b). As a result, we hypothesize that the waves almost always "feel" the ripples, and that the wave boundary layer remains hydraulically rough. Even in the absence of waves, the isotropic roughness at the fine site makes it unlikely that the sediment characteristics ever set the roughness ($k_s \sim D_{50}$), even for mean flow that parallels the ripple crests. Assuming $k_s \sim 30z_{0,}$ but neglecting the orientation of the ripples (equation (8)) results in values of R_* that are always above 70 at the fine site, consistent with hydraulically rough flow.

We cannot rule out the possibility that the higher variability in drag inferred at the coarse site is the result of our measurements being influenced by near bed coherent vortices induced by the large orbital ripples at this location. Laboratory studies demonstrate that oscillatory currents over a rippled bed generate a coherent vortex that affects the horizontal distribution of the turbulence in the region immediately adjacent to the bed (Hare et al., 2014; Rodríguez-Abudo et al., 2013). In this region, the turbulence statistics vary horizontally and estimates of the bed stress could depend on the location of the measurements relative to the ripple morphology. Jiménez (2004) suggests that the effect of this coherent motion is limited to the region where $z < \eta \min[1+\lambda/\eta, 5]$. During both deployments, the measurement height of the ADV sampling volume is never lower than this proposed threshold, consistent with the assumption that our turbulence measurements represent the integrated effect of the underlying roughness at scales larger than the individual ripples. However, the interactions between oscillatory and mean currents are poorly understood and these motions could extend further into the water column when both mean currents and wave motions are present. However, we note that our measurements represent many realizations, with many different locations relative to the individual ripples. Furthermore, consistent with atmospheric flux measurements, the turbulent statistics we observe most likely represent a spatial footprint that integrates over a streamwise distance much larger than the individual ripple spacing (e.g., Kljun et al., 2004). Thus, we do not think this is the primary source of the observed variability.

6. Conclusions

The direct covariance measurements of mean stress presented above are largely consistent with the enhancement of drag due to wave-current interaction proposed by GM-79, provided the appropriate roughness length is known. Data collected at two locations, including one coarse site with large orbital ripples and one fine site with smaller sub-orbital ripples, highlight the complexity of quantifying this roughness. Images of the seabed from a rotary sonar suggest fundamental differences between the response of the seabed at the two locations. Roughness generally increases with wave forcing at the coarse site, whereas the roughness appears to decrease under increased wave forcing at the fine site, consistent with equilibrium ripple models. The ripple crests at the fine site are oriented at a significant angle to the bathymetry, whereas the crests of the ripples at the coarse site are much more parallel to the bathymetry. The orbital ripples at the coarse site are largely 2-dimensional resulting in anisotropic roughness. The sub-orbital ripples at the fine site are more 3-dimensional with more isotropic roughness. Finally, the large orbital ripples at the coarse site are often not in equilibrium with the wave forcing resulting in relic ripples that have wavelengths that are long compared to the wave orbital diameter ($\lambda > d_0$), while the sub-orbital ripples at the fine site often have $\lambda < d_0$.

These differences in the characteristics and response of the seabed lead to some important differences in the drag experienced at the two locations, including the paradoxical result that the site with larger ripples experiences lower drag, on average. At the coarse site, the drag is much more sensitive to the relative orientation of the current to the ripple crests, with flows parallel to the crests having markedly lower drag. There are two potential explanations for this difference. First, as noted above, the reduced sensitivity at the fine site could simply reflect the more heterogeneous roughness at this site. Second, there is evidence to suggest that flow at the coarse site is not always hydraulically rough. The low values of C_d at the coarse site occur during conditions when the mean current is oriented roughly parallel to the ripple crests and when large relic ripples are present ($\lambda > d_0$). Our data suggest that for these conditions, the wave boundary layer may no longer be turbulent and the mean current experiences sufficiently small roughness for the flow to become hydraulically smooth with roughness that is consistent with $z_0 \sim \nu/(9u_{*c})$. This transition to hydraulically smooth flow does not appear to happen at the fine site for several reasons. First, for the sub-

orbital ripples observed at this location, the orbital diameter is almost always bigger than the ripple wavelength, which we hypothesize results in a wave-boundary layer that is always fully turbulent. Second, the smaller ripples at the fine site are more 3-dimensional so the mean current never experiences a roughness sufficiently small for $R_* < 70$.

The results presented here are generally consistent with existing boundary layer models, but only after accounting for a number of complex processes. In addition to highlighting the importance of wave-current interaction, these data demonstrate the important contributions to variations in drag that are caused by nonequilibrium ripple dynamics, ripple anisotropy, the orientation of the ripples relative to the mean current and the turbulent state of the oscillatory wave boundary layer. These processes all contribute to bottom drag that is highly variable in both time and space. Such variations almost certainly play an important role in both circulation and sediment transport on the continental shelf. All of these processes can be included in regional-scale numerical simulations of coastal circulation, but only if accurate information about the state of the seabed is known.

Acknowledgments
The authors thank the captains and crews of the R/V Connecticut and the R/V Tioga, and the field teams from Woods Hole Oceanographic Institution and the U.S. Geological Survey, especially Jay Sisson, Andy Davies, Marinna Martini, Jon Borden, Ellyn Montgomery, Pat Dickhudt, and Sandra Brosnahan. This research was supported by National Science Foundation Ocean Sciences Division Award 1356060 and the U.S. Geological Survey Coastal and Marine Geology Program. Any use of trade, firm, or product names is for descriptive purposes only and does not imply endorsement by the U.S. Government. The field measurements have been archived (Montgomery et al., 2016) and are publicly available at https://stellwagen.er.usgs.gov/mvco_14.html

References

Agrawal, Y. C., & Traykovski, P. (2001). Particles in the bottom boundary layer: Concentration and size dynamics through events. *Journal of Geophysical Research*, *106*, 9533–9542. https://doi.org/10.1029/2000JC900160

Barrantes, A. I., & Madsen, O. S. (2000). Near-bottom flow and flow resistance for currents obliquely incident to two-dimensional roughness elements. *Journal of Geophysical Research*, *105*, 26253–26264.

Clifton, H. E., & Dingler, J. R. (1984). Wave-formed structures and paleoenvironmental reconstruction. *Marine Geology*, *60*, 165–198.

Conley, D. C., & Inman, D. L. (1994). Ventilated oscillatory boundary layers. *Journal of Fluid Mechanics*, *273*, 261–284.

Davies, A. M., & Lawrence, J. (1995). Modeling the effect of wave–current interaction on the three-dimensional wind-driven circulation of the Eastern Irish Sea. *Journal of Physical Oceanography*, *25*(1), 29–45.

Drake, D. E., Cacchoine, D. A., & Grant, W. D. (1992). Shear stress and bed roughness estimates for combined wave and current flows over a rippled bed. *Journal of Geophysical Research*, *97*, 2319–2326.

Ganju, N. K., & Sherwood, C. R. (2010). Effect of roughness formulation on the performance of a coupled wave, hydrodynamic, and sediment transport model. *Ocean Modelling*, *33*, 299–313.

Gargett, A., Wells, J., Tejada-Martınez, A. E., & Grosch, C. E. (2004). Langmuir supercells: A mechanism for sediment resuspension and transport in shallow seas. *Science*, *306*, 1925–1928.

Gargett, A. E., & Wells, J. R. (2007). Langmuir turbulence in shallow water. Part 1. Observations. *Journal of Fluid Mechanics*, *576*, 27–61.

Glenn, S. M., & Grant, W. D. (1987). Suspended sediment stratification correction for combined wave and current flows. *Journal of Geophysical Research*, *92*, 8244–8264.

Goff, J. A., Mayer, L. A., Traykovski, P., Buynevich, I., Wilkens, R., Raymond, R., et al. (2005). Detailed investigation of sorted bedforms, or "rippled scour depressions," within the Martha's Vineyard Coastal Observatory, Massachusetts. *Continental Shelf Research*, *25*(4), 461–484.

Grant, W. D., & Madsen, O. S. (1979). Combined wave and current interaction with a rough bottom. *Journal of Geophysical Research*, *84*, 1797–1808.

Grant, W. D., & Madsen, O. S. (1982). Moveable bed roughness in unsteady oscillatory flow. *Journal of Geophysical Research*, *87*, 469–481.

Grant, W. D., & Madsen, O. S. (1986). The continental-shelf bottom boundary layer. *Annual Review of Fluid Mechanics*, *18*, 265–305.

Grant, W. D., Williams, A. J., III., & Glenn, S. M. (1984). Bottom stress estimates and their predictions on the northern California continental shelf during CODE-1: The importance of wave-current interaction. *Journal of Physical Oceanography*, *14*, 506–527.

Green, M., Rees, J., & Pearson, N. D. (1990). Evidence for the influence of wave-current interaction in a tidal boundary layer. *Journal of Geophysical Research*, *95*, 9629–9644.

Gross, T. F., Isley, A. E., & Sherwood, C. R. (1992). Effective roughness changes during storms on the Northern California shelf. *Continental Shelf Research*, *12*, 389–414.

Gross, T. F., Williams, A. J., & Terray, E. A. (1994). Bottom boundary layer spectral dissipation estimates in the presence of wave motions. *Continental Shelf Research*, *14*, 1239–1256.

Hackett, E., Luznik, L., Katz, J., & Osborn, T. R. (2009). Effect of finite spatial resolution on the turbulent energy spectrum measured in the coastal ocean bottom boundary layer. *Journal of Atmospheric and Oceanic Technology*, *26*, 2610–2625.

Hare, J., Hay, A. E., Zedel, L., & Cheel, R. (2014). Observations of the space-time structure of flow, turbulence, and stress over orbital-scale ripples. *Journal of Geophysical Research: Oceans*, *119*, 1876–1898. https://doi.org/10.1002/2013JC009370

Hay, A. E. (2008). Near-bed turbulence and relict waveformed sand ripples: Observations from the inner shelf. *Journal of Geophysical Research*, *113*, C04040. https://doi.org/10.1029/2006JC004013

Hay, A. E., & Mudge, T. (2005). Principal bed states during SandyDuck97: Occurrence, spectral anisotropy, and the bed state storm cycle. *Journal of Geophysical Research*, *110*, C03013. https://doi.org/10.1029/2004JC002451

Huntley, D. (1988). A modified inertial dissipation method for estimating seabed stresses at low Reynolds numbers, with application to wave/current boundary layer measurements. *Journal of Physical Oceanography*, *18*, 339–346.

Jiménez, J. (2004). Turbulent flows over rough walls. *Annual Review of Fluid Mechanics*, *36*, 173–196.

Jones, K., & Traykovski, P. (2018). A method to quantify bedform height and asymmetry from a low-mounted sidescan sonar. *Journal of Atmospheric and Oceanic Technology.* https://doi.org/10.1175/JTECH-D-17–0102.1

Kljun, N., Calanca, P., Rotach, M. W., & Schmid, H. P. (2004). A simple parameterisation for flux footprint predictions. *Boundary-Layer Meteorology*, *112*(3), 503–523.

Lentz, S., Guza, R. T., Elgar, S., Feddersen, F., & Herbers, T. H. C. (1999). Momentum balances on the North Carolina inner shelf. *Journal of Geophysical Research*, *104*, 18205–18226.

Luznik, L., Gurka, R., Zhu, W., Nimmo Smith, W. A. M., Katz, J., & Osborn, T. R. (2007). Distributions of energy spectra, Reynolds stresses, turbulence production and dissipation in a tidally driven bottom boundary layer. *Journal of Physical Oceanography*, *37*, 1527–1550.

Madsen, O. S., Poon, Y.-K., & Graber, H. C. (1988). Spectral Wave attenuation by bottom friction: Theory. Paper presented at the 21st International Conference on Coastal Engineering, American Society of Civil Engineering, New York.
Malarkey, J., & Davies, A. G. (2003). A non-iterative procedure for the Wiberg and Harris (1994) oscillatory sand ripple predictor. *Journal of Coastal Research*, *19*, 738–739.
Montgomery, E. T., Sherwood, C. R., Martini, M. A., Trowbridge, J., Scully, M., & Brosnahan, S. M. (2016). Oceanographic and water-quality measurements collected south of Martha's Vineyard, MA, 2014–2015. U.S. Geological Survey data release. https://doi.org/10.5066/F7542KQR
Nelson, T. R., Voulgaris, G., & Traykovski, P. (2013). Predicting wave-induced ripple equilibrium geometry. *Journal of Geophysical Research: Oceans*, *118*, 3202–3220. https://doi.org/10.1002/jgrc.20241
Nimmo-Smith, W., Atsavapranee, P., Katz, J., & Osborn, T. (2002). PIV measurements in the bottom boundary layer of the coastal ocean. *Experiments in Fluids*, *33*, 962–971.
Rodríguez-Abudo, S., Foster, D. L., & Henriquez, M. (2013). Spatial variability of the wave bottom boundary layer over movable rippled beds. *Journal of Geophysical Research: Oceans*, *118*, 3490–3506. https://doi.org/10.1002/jgrc.20256
Sherwood, C. R. (2011). Directional bottom roughness associated with waves, currents, and ripples: Coastal Sediments '11. In Rosati, J., Wang, P., & Roberts, T. (Eds.,) *Proceedings of the Seventh International Symposium on Coast Engineering and Science of Coastal Sediment Processes* (13 pp.). Miami, FL: World Scientific Publishing Company.
Sherwood, C. R., Lacy, J. R., & Voulgaris, G. (2006). Shear velocity estimates on the inner shelf off Grays Harbor, Washington, USA. *Continental Shelf Research*, *26*(17–18), 1995–2018. https://doi.org/10.1016/j.csr.2006.07.025
Signell, R. P., Beardsley, R. C., Graber, H. C., & Capotondi, A. (1990). Effect of wave-current interaction on wind-driven circulation in narrow, shallow embayments. *Journal of Geophysical Research*, *95*, 9671–9678.
Soulsby, R. (1997). *Dynamics of marine sands: A manual for practical applications* (249 pp.). London, UK: Thomas Telford.
Styles, R., & Glenn, S. M. (2000). Modeling stratified wave and current bottom boundary layers on the continental shelf. *Journal of Geophysical Research*, *105*, 24119–24139.
Styles, R., & Glenn, S. M. (2002). Modeling bottom roughness in the presence of wave-generated ripples. *Journal of Geophysical Research*, *107*(C8), 3110. https://doi.org/10.1029/2001JC000864
Tejada-Martinez, A. E., Grosch, C. E., Sinha, N., Akan, C., & Martinat, G. (2012). Disruption of the bottom log layer in large-eddy simulations of full-depth Langmuir circulation. *Journal of Fluid Mechanics*, *699*, 79–93.
Traykovski, P. (2007). Observations of wave orbital scale ripples and a nonequilibrium time-dependent model. *Journal of Geophysical Research*, *112*, C06026. https://doi.org/10.1029/2006JC003811
Traykovski, P., Hay, A. E., Irish, J. D., & Lynch, J. F. (1999). Geometry, migration, and evolution of wave orbital ripples at LEO-15. *Journal of Geophysical Research*, *104*, 505–1524.
Trembanis, A. C., Wright, L. D., Friedrichs, C. T., Green, M. O., & Hume, T. (2004). The effects of spatially complex inner shelf roughness on boundary layer turbulence and current and wave friction: Tairua embayment, New Zealand. *Continental Shelf Research*, *24*(13), 1549–1571.
Trowbridge, J. H. (1998). On a technique for measurement of turbulent shear stress in the presence of surface waves. *Journal of Atmospheric and Oceanic Technology*, *15*, 290–298.
Trowbridge, J. H., & Elgar, S. (2001). Turbulence measurements in the surf zone. *Journal of Physical Oceanography*, *31*, 2403–2417.
Trowbridge, J. H., & Elgar, S. (2003). Spatial scales of stress-carrying nearshore turbulence. *Journal of Physical Oceanography*, *33*, 1122–1128.
Trowbridge, J. H., & Kineke, G. C. (1994). Structure and dynamics of fluid muds on the Amazon continental shelf. *Journal of Geophysical Research*, *99*, 865–874.
Trowbridge, J. H., & Lentz, S. (2017). The bottom boundary layer. *Annual Review of Marine Sciemces*, *10*, 397–420. https://doi.org/10.1146/annurev-marine-121916-063351
Trowbridge, J. H., Scully, M. E., & Sherwood, C. R. (2018). The cospectrum of stress-carrying turbulence in the presence of surface waves. *Journal of Physical Oceanography*, *48*(1), 29–44.
Wiberg, P., & Smith, J. D. (1983). A comparison of field data and theoretical models for wave-current interactions at the bed on the continental shelf. *Continental Shelf Research*, *2*, 147–162.
Wiberg, P. L., & Harris, C. K. (1994). Ripple geometry in wave-dominated environments. *Journal of Geophysical Research*, *99*, 775–789.
Xie, L., Wu, K., K.,Pietrafesa, L., & Zhang, C. (2001). A numerical study of wave-current interaction through surface and bottom stresses: Wind-driven circulation in the South Atlantic Bight under uniform winds. *Journal of Geophysical Research*, *106*, 16841–16855.